Engineering and Technology Journal
Journal homepage: https://etj.uotechnology.edu.iq

Sustainable geopolymer concrete: Iraqi steel slag as a high-performance aggregate for improved strength and durability

Riyam I. Jaddan[a,b*], **Hussein A. Jaber**[a]

[a] Materials Engineering Dept., University of Technology-Iraq, Alsina'a street, 10066 Baghdad, Iraq.
[b] Department of Materials Engineering, College of Engineering, University of Al-Qadisiyah, 58001, Al-Diwaniyah, Iraq.
*Corresponding author Email: mae.22.037@grad.uotechnology.edu.iq

HIGHLIGHTS

- Valorization of Iraqi steel slag reduced landfill waste and natural aggregate consumption.
- A novel synergy between low-calcium metakaolin and steel slag was achieved.
- Using 30% steel slag aggregate increased geopolymer strength to 95.1 MPa.
- Steel slag aggregate provided 11.3 MPa flexural strength in geopolymer composites.
- Porosity was reduced by 26.32%, enhancing durability in aggressive environments.

Keywords:

Steel slag
Geopolymer concrete
Metakaolin
Waste material
Alkali activator.

ABSTRACT

The construction industry's reliance on ordinary Portland cement (OPC) contributes significantly to CO_2 emissions and resource depletion. Geopolymer concrete (GPC) offers a sustainable alternative, but natural aggregates (NAs) still harm the environment. This study investigates recycled coarse steel slag aggregate (RCSA), a metallurgical byproduct, as a partial replacement (10, 20, 30, and 40% by volume) for natural coarse aggregate (NCA) in metakaolin-based GPC. The geopolymer paste was formulated with optimal molar ratios of 3.65 for SiO_2/Al_2O_3, 2.9 for sodium hydroxide/sodium silicate, and 0.62 for water/metakaolin. Results showed that incorporating RCSA enhances both mechanical and physical properties of GPC. Optimal performance was achieved with a 30% RCSA substitution, showing remarkable improvements over conventional GPC at 28 days of curing: a 29.56% increase in compressive strength (95.1 MPa vs. 73.4 MPa), along with 26.12 and 41.07% enhancements in splitting tensile and flexural strengths, respectively. Bulk density increased by 8.15% (2371.96 kg/m³ vs. 2193.12 kg/m³). In comparison, physical analysis revealed a 26.32% reduction in porosity and a 9.18% decrease in water absorption, indicating improved interfacial transition zone (ITZ) between the RCSA and geopolymer paste, facilitated by calcium leaching from the slag particles, which promotes densification and reduced permeability. Microstructural analyses (XRD and FTIR) confirmed successful geopolymerization and a robust amorphous geopolymer network. Findings confirm RCSA mitigates environmental impacts through waste valorization and significantly enhances GPC performance, offering a viable pathway toward more sustainable construction materials.

1. Introduction

Nowadays, the most utilized material in the construction industry is concrete, accounting for around 30 billion tons of global consumption annually [1]. However, this extensive utilization demands vast quantities of ordinary Portland cement (OPC), which serves as the primary binder in conventional concrete. Consequently, the cement industry faces significant environmental challenges, including the intensive depletion of natural resources [2,3], excessive energy consumption [4], and substantial greenhouse gas emissions [5]. For instance, producing one ton of cement typically requires approximately 1.5 tons of raw materials, resulting in the direct emission of about 0.65–0.92 tons of CO_2. Additionally, fuel combustion during the production process generates nearly 0.4 tons of CO_2, bringing the total emissions to 0.8–1.0 tons of CO_2 per ton of cement produced [6,7]. Moreover, the cement industry also consumes a considerable amount of fossil fuels, accounting for roughly 12–15% of industrial energy consumption globally. Collectively, greenhouse gas emissions from cement production amount to approximately 1.35 billion tons annually, contributing to 6–9% of global emissions [8]. Owing to its profound impact on waste mitigation, drastic carbon dioxide emission reduction, exceptional durability, and superior eco-compatibility, low-carbon concrete, commonly termed geopolymer concrete, is heralded as a revolutionary and environmentally superior substitute for Portland cement in the construction sector [9-11]. Geopolymer, a groundbreaking creation born from the mind of scientist Joseph Davidovits in 1972, shatters conventions with its audacious reliance on natural resources and industrial refuse as primary ingredients. These unconventional raw materials undergo a transformative alchemical process through alkali or acid activation, forging a binder, an

http://doi.org/10.30684/etj.2025.161902.1976
Received 22 June 2025; Received in revised form 08 August 2025; Accepted 15 August 2025; Available online 25 September 2025
2412-0758/University of Technology-Iraq, Baghdad, Iraq

alkaline aluminosilicate [12]. This exothermic reaction, a dramatic interplay between aluminosilicate and alkali, summons the geopolymer into existence [13]. Defying the need for searingly high temperatures, this revolutionary material solidifies stoically at room temperature, slashing CO_2 emissions and eclipsing traditional inorganic polymers. Geopolymer strides boldly as a fierce and eco-conscious successor to cement, embodying the future of sustainable innovation.

Furthermore, the extensive use of concrete by humans also contributes to another ecological problem: the depletion of natural aggregates. Natural aggregates (NAs) remain the primary aggregate component in both cement concrete and Geopolymer concrete. There is significant demand for them in concrete Preparation, as the concrete comprises 75 to 80 percent of aggregates in its total volume. The massive demand for concrete has led to the over-exploitation of NA, which has caused resource depletion in some areas and ecological damage [14]. It is significant to find alternatives to NAs while considering the environment, resources, and economic factors during the decision-making process. Additionally, there are hurdles facing the unreasonable disposal and handling of the large amount of waste material, which manifests from the growth in human activities that generate a large amount of solid waste across diverse sectors, such as the production of power, the production of iron and steel, the production of electronic goods, and industrial production [15].

Slag is a formidable byproduct generated from the high-temperature, rigorous metallurgical processes involved in metal smelting and refining [16,17]. Amassed a staggering 1878.5 million tons in 2022 alone, Prudent appraisals of steel slag generation surpass 225 million tons [18]. This abysmal utilization precipitates rampant stockpiling, engendering deleterious ramifications for ecological preservation [19,20]. A substantial fraction of steel slag remains unutilized promptly, necessitating landfilling or open-air deposition, thereby expropriating vast tracts of arable land. Moreover, steel slag contains a diverse array of hazardous heavy metal elements that may leach and permeate soil and aquatic environments, posing significant ecotoxicological threats and potential risks to human health [21-24]. When steel slag is piled up outside or handled carelessly during transport, it creates dust pollution. This dust makes air quality worse and can cause serious breathing problems for people [25]. One potential mitigation strategy involves using steel slag as an admixture for partial replacement of cement in concrete. However, the application of steel slag as a cementitious material is limited by its low pozzolanic activity, which is primarily attributed to its high iron oxide content and low amorphous silica content [26-28]. An alternative and more viable approach is to utilize steel slag as an aggregate in concrete. Steel slag contains substantial amounts of free lime (CaO) and periclase (MgO), which can hydrate to form calcium hydroxide and magnesium hydroxide, respectively. This hydration process results in delayed volumetric expansion, with increases of approximately 98% for free lime and 148% for free periclase [29]. The calcium hydroxide produced in this case differs from that generated by cement hydration in terms of morphology, with the former displaying irregular, large, and massive crystals. At the same time, the latter is characterized by a regular, layered, or sheet-like structure [30]. This allows sufficient space for the growth of ettringite; the proliferation of ettringite exacerbates crack propagation, thereby facilitating the ingress of water into the concrete and intensifying the expansion of steel slag. The persistent formation of calcium hydroxide and ettringite crystals culminates in the eventual degradation of the concrete, manifesting as cracking and spalling, or, in severe cases, structural failure if not adequately controlled [31-33].

To address this issue, steel slag aggregates with reduced particle size and increased fineness achieved through grinding have been utilized to expedite the hydration of these oxides [34,35]. However, the high hardness of the steel slag enhances the incidence of mill faults, resulting in elevated costs for equipment maintenance and replacement. Furthermore, the poor grinding performance and the high energy consumption limit the use of steel slag as a powder [36]. In light of the foregoing, the incorporation of steel slag aggregate into GPC emerges as a promising strategy, offering advantages such as reduced energy consumption, inhibition of the leaching of heavy metals, and lower production costs. Several studies have explored the use of steel slag aggregates in GPC as a sustainable alternative to NAs. In the work of Omar et al., it was found that replacing NAs with steel slag in fly ash-based GPC improved compressive strength (up to 23%), flexural strength (9%), and tensile strength (19%), while reducing water absorption (3–5%) and permeable voids (8–12%) [37]. In a similar vein, Khan et al. demonstrated that steel furnace slag in low-calcium fly ash GPC enhanced compressive strength and surface resistivity, with EDS analysis confirming calcium diffusion from slag aggregate into the geopolymer paste, preventing expansion, enhancing the interfacial transition zone (ITZ) [38]. Building on this, Mahmood et al., developed high-density GPC made with fly ash and granulated blast furnace slag (GGBS) (2600–2630 kg/m³) using steel slag aggregate, achieving 37 MPa compressive strength, 2.5–5.5 MPa tensile strength, and 30.3 GPa elastic modulus, with microstructural analysis confirming strong ITZ due to Ca diffusion [39,40]. In addition, Suganya et al. [41], reported that GPC based on fly ash and GGBS with coarse steel slag aggregate exhibited 5.2% higher compressive strength and superior durability against acid/sulfate attacks compared to conventional concrete. Moreover**,** Amani et al. [42], observed that electric arc furnace slag (EAFS) in GGBS-based GPC reduced compressive strength (5–25%) but improved tensile strength (3.8%) and modulus of rupture (16.67%), alongside environmental benefits.

Despite the significant progress in research, most studies have primarily focused on GPC made with fly ash and GGBS, which contain moderate to high calcium content, potentially limiting free lime diffusion from steel slag. This study introduces a novel approach by exploring explores the utilization of locally sourced Nano metakaolin to produce GPC incorporating recycled coarse steel slag aggregate. To the best of our knowledge, the specific combination of low-calcium metakaolin-based geopolymer concrete with RCSA has not been extensively investigated. This research fills a critical gap by demonstrating the feasibility and enhanced performance of this unique material combination, offering a more sustainable and high-performance alternative for the construction industry. Our work provides new insights into the interfacial transition zone (ITZ) development and overall material properties when RCSA is incorporated into a metakaolin-based geopolymer matrix.

2. Experimental work

2.1 Materials

2.1.1 Metakaolin

$Al_2Si_2O_5(OH)_4$ Nano Iraqi kaolin, sourced from the nearby region of "Al-Mishraq (Mosul, Iraq)," was utilized as the primary precursor material. Crystalline kaolin was converted to amorphous Metakaolin (MK-800) via calcination at 800° for three hours with a 5 °C/min heating rate [43, 44]. The processed material was then stored in glass containers to prevent exposure to humidity. A particle size analyzer (PZA) was employed to measure the particle size of the MK-800 powder, as shown in Figure 1. It can be seen that MK-800 has a typical particle size of 93.4 nm. The chemical composition of kaolin and MK-800 coducting through X-ray fluorescence (XRF), as shown in Table 1.

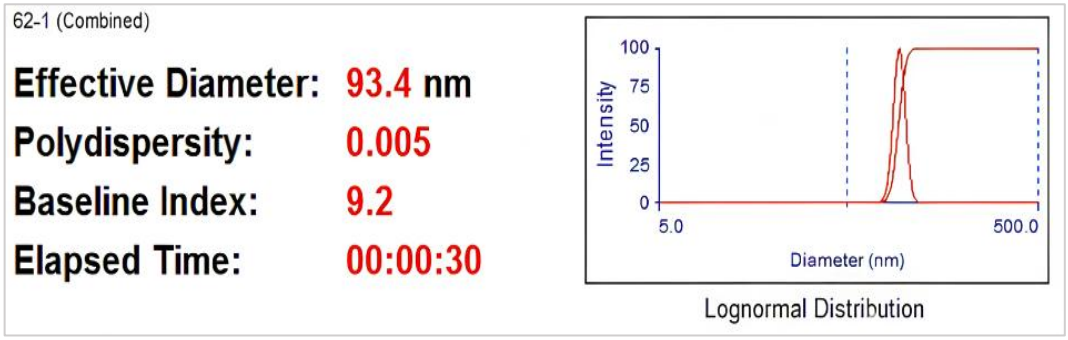

Figure 1: MK-800 particle size analyzer

Table 1: The Kaolin and Metakaolin XRF analysis results

Oxide %	K_2O%	Na_2O%	CaO%	Al_2O_3%	MgO%	SiO_2%	Fe_2O_3%	TiO_2%	SO_3%
MK	0.406	0.167	0.554	27.27	0.13	40.89	1.447	1.654	0.225
MK-800	0.527	0.087	0.619	31.51	0.11	45.81	1.824	2.03	0.275

2.1.2 Alkaline solution

Commercial-grade sodium hydroxide (SS) (NaOH) flake and sodium silicate (SH) (Na_2SiO_3) solution were utilized as alkali activators, owing to their superior commercial accessibility and cost-effectiveness relative to potassium-based counterparts [45], as duplicated in Table 2, with 16M of SH and an SS/SH ratio of 2.6.

Table 2: Properties of alkaline activators

Properties	Sodium silicate	Sodium hydroxide
Chemical formula	Na_2SiO_3	NaOH
Na_2O%	13.5	N/A
SiO_2%	32.5	N/A
H_2O%	54	N/A
NaOH%	N/A	N/A
Na_2CO_3%	N/A	0.54
Appearance	Hazy	flakes like shape, white

2.1.3 Aggregates

Natural sand sourced from the AL-Akhaidhir area was utilized as the natural fine aggregate (NFA) in this study. Based on the results of the sieve analysis and physical properties presented in Table 2, the sand conforms to Zone (2) classification as per the Iraqi Standard No. 45/2016 [46], as duplicated in Table 3.

Table 3: Physical properties and sieve analysis of fine aggregate from the AL-Akhaidhir area

Sieve size (mm)	Passing (%)	Limits of Iraqi Standard No.45, Zone (2) [46]
10	100	100
4.75	96	90-100
2.36	80	75-100
1.18	64	55-90
0.3	15.8	8-30
Physical properties	**Value**	**Limits of Iraqi Standard No.45/2016 Zone (2)**
Specific Gravity	2.58	--
Absorption, (%)	2.5	--
Sulfate Content (SO_3) (%)	0.09	≤0.1

Naturally crushed coarse aggregate (maximum size 12 mm) from the Al-Nibaai region was utilized. Table 4 shows its properties, confirming compliance with Iraqi Standard No. 45/2016 for grading and sulfate content [46], as duplicated in Table 4.

Table 4: Physical properties and sieve analysis of coarse aggregate

Sieve size (mm)	**Passing (%)**	**Limits of Iraqi Standard No. 45 with (5- 12) mm [46]**
12	100	100
10	98	100-95
5	35	30-60
2.36	1	0-10
Physical properties	**value**	**Limits of Iraqi Standard No. 45/ 2016**
Specific Gravity	2.56	--
Absorption, (%)	1.92	--
Sulfate Content (SO_3), (%)	0.09	≤0.1
Dry Density, (kg/m³)	1740	--

Recycled Coarse Steel Slag Aggregate (RCSA) from SGR Company in Basra was used as a volumetric replacement for NCA in GPC, as shown in Figure 2. According to Iraqi Specification No. 45/2016, it was crushed and sieved to meet the grading of the natural aggregate [46]. Chemical compositions have been analyzed using X-ray fluorescence (XRF), as shown in Table 5.

Figure 2: RCSA

Table 5: Physical, chemical properties, and sieve analysis of (RCSA)

Sieve size (mm)					**Passing (%)**		**Limits of Iraqi specification No. 45 [46]**		
12					100		100		
10					95		95-100		
5					56		30-60		
2.36					7		0-10		
property					**Value**				
Density (kg/m³)					2900				
Absorption %					2.3				
Specific gravity					3.31				
Sulfate content (SO_3) %					0.53				
Oxide%	**K_2O%**	**Na_2O%**	**CaO%**	**Al_2O_3%**	**MgO%**	**SiO_2%**	**Fe_2O_3%**	**TiO_2%**	**SO_3%**
RCSA	0.0487	0.000	23.57	3.278	2.355	19.08	37.53	0.5574	0.5

2.2 Mix procedure and specimens preparation

The geopolymer paste was formulated based on preliminary experimental investigations (unpublished data), which determined optimal molar ratios of 3.65 for SiO_2/Al_2O_3, 2.9 for SS/SH, and 0.62 w/MK. The mix design parameters for the GPC specimens are detailed in Table 6. Five distinct mixtures were designed with progressive replacement levels of NCA by RCSA: 0RCSA (0% replacement, 10RCSA (10%), 20RCSA (20%), 30RCSA (30%), and 40RCSA (40%), where all substitutions were performed on a volumetric basis. A constant water content was maintained for all mixes based on preliminary tests to optimize geopolymer paste molar ratios. This controlled ratio ensured consistent geopolymerization, allowing changes in GPC properties to be attributed mainly to varying RCSA content rather than water or alkaline solution variations.

SH was completely dissolved in the required volume of water. The solution was then cooled to room temperature, after which SS was added and stirred at 600 rpm. Before use as a binding agent, the solution was heat-treated at 85 °C for 20 minutes and then allowed to rest at room temperature for 24 hours, as can be seen in Figure 3a. The heat treatment facilitated the breakdown of SS chains by SH, generating a higher number of oligomers to promote the formation of a 3D geopolymer network. After 24 hours, the required amount of MK-800 was added to the cooled alkaline activator solution. The mixture was then blended using an overhead mixer at a constant speed of approximately 3000 rpm for 5 min to achieve a homogeneous geopolymer cement paste, as can be seen in Figure 3b.

Table 6: Details of GPC Mixes*

Mix Name	MK-800 (Kg/m^3)	SS (kg)	SH (kg)	NFA (kg/m^3)	Coarse aggregate		Water (Kg/m^3)
					NCA (kg/m^3)	RCSA (kg/m^3)	
0RCSA	209	198	17.39	600	1100	0	25.6
10RCSA	209	198	17.39	600	990	141.13	25.6
20RCSA	209	198	17.39	600	880	282.27	25.6
30RCSA	209	198	17.39	600	770	423.4	25.6
40RCSA	209	198	17.39	600	660	564.5	25.6

*, SS: Sodium Silicate, SH: Sodium Hydroxide, NFA: Natural Fine Aggregate, NCA: Natural Coarse Aggregate, RCSA: Recycled Coarse Steel Slag Aggregate.

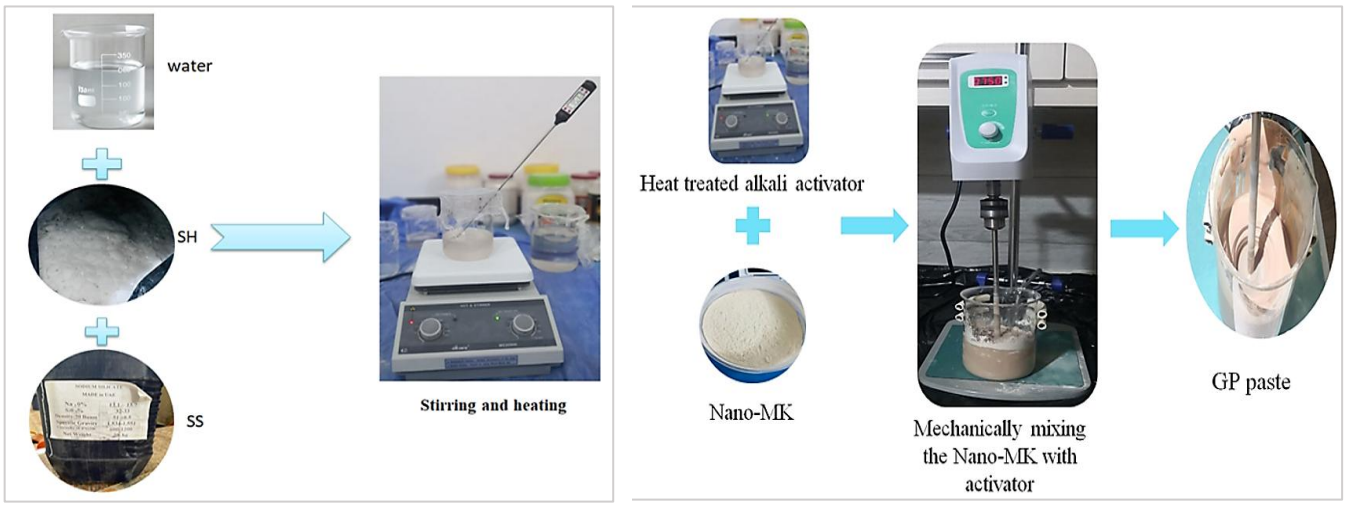

Figure 3: a) Alkali activator preparation, b) GP paste preparation

After determining the mixing proportions, the sand and both NCA and RCSA were first blended in their dry state at low speed until a uniform mixture was achieved, with mixing continued for at least one minute. Subsequently, a medium-speed mixing regime was initiated while the GP paste was gradually incorporated. Finally, the mixture was further processed at high speed for 5–10 minutes to ensure a homogeneous and well-dispersed fresh mixture.

The prepared GPC was then poured into the required molds for testing. To prevent excessive water evaporation and ensure optimal geopolymerization, all specimens were sealed with polyethylene film. Demold after 24 hours and let the specimens sit at ambient temperature (25 °C) until the day of testing. This curing method not only simplifies geopolymer application but also enhances cost efficiency by eliminating the need for external heating [47].

2.3 Testing methodology

The microstructural characteristics of the component ingredients and the resultant geopolymer were thoroughly evaluated. Advanced characterization techniques, including Fourier-transform infrared spectroscopy (FTIR) and X-ray diffractometry (XRD), were employed to analyze the powder compositions.

The experimental program in this study involved rigorous testing of hardened concrete at 7 and 28 days curing intervals. Three specimens were tested for each evaluation to ensure statistical reliability. The relevant testing standards, methodological specifications, and sample dimensions for GP-RCSA assessments are summarized in Table 7.

Table 7: Tests for hardened GP-RCSA evaluation

Properties	Molds dimensions	Testing standard
	Mechanical properties	
Compressive strength	Cube (100 mm side)	BS 1881-Part 116 [48]
Flexural Strength	Prism (100 mm×100 mm×400 mm)	ASTM C293 [49]
Split Tensile strength	100 Ø × 200 mm cylinder	ASTM C496 [50]
	Physical properties	
Bulk density	Cube (100 mm side)	BS EN 12390-7 [51]
	Durability properties	
Water absorption	Cube (100 mm side)	ASTM C642 [52]
Volume of Permeable Voids	Cube (100 mm side)	ASTM C642 [52]

3. Results and discussion

3.1 XRD Patterns

The mineralogical composition of the kaolin, metakaolin, and steel slag aggregate was determined using X-ray diffraction (XRD). Figure 4 presents the XRD results for kaolin and metakaolin, highlighting the characteristic peaks identified using standard ICCD patterns: 00-033-1161 for quartz and 00-001-0527 for kaolinite.

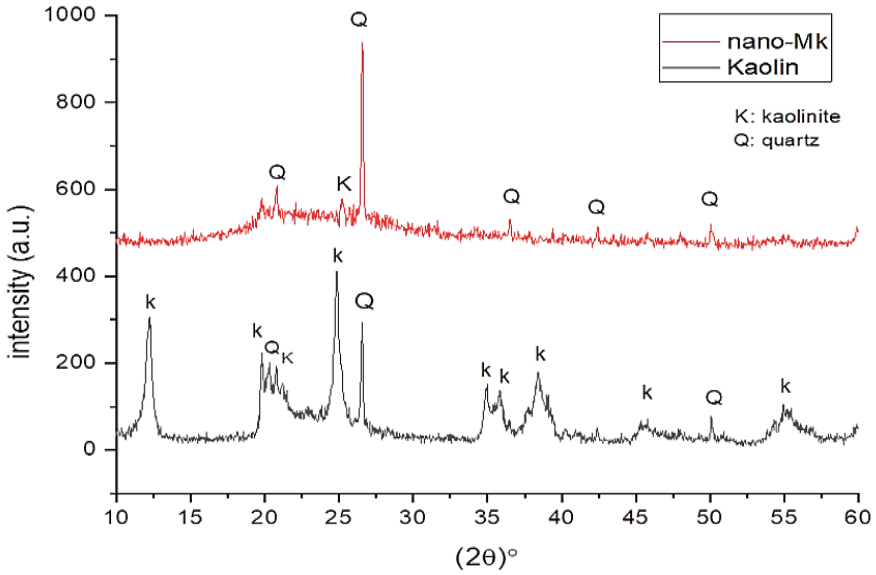

Figure 4: X-ray diffraction of kaolin and MK-800

The XRD examination of the kaolin sample revealed distinct diffraction peaks corresponding to both kaolinite and quartz phases. The characteristic peaks for kaolinite were observed at 12.32°, 20.10°, 24.88°, 35.00°, 38.40°, 45.00°, 55.50°, and 62.32°. Additionally, significant peaks at 20.80°, 26.56°, 50.08°, and 54.88° were identified, corresponding to the quartz phase, indicating a high degree of crystallinity. The XRD pattern of MK-800 showed a predominantly amorphous profile, with the absence of most kaolinite peaks; only a residual peak at 24.88° was observed. However, several peaks attributed to quartz were still present at 20.80°, 26.52°, 36.56°, 42.48°, and 50.16°. This diffraction pattern confirms the successful transformation of kaolin into amorphous metakaolin, while also indicating the presence of crystalline free silica (quartz) as evidenced by the sharp peaks. Also, Figure 5 shows the XRD patterns of steel slag aggregate, which exhibit a complex multiphase composition, characterized by numerous overlapping peaks indicative of a heterogeneous mixture of crystalline phases commonly observed in steel slags.

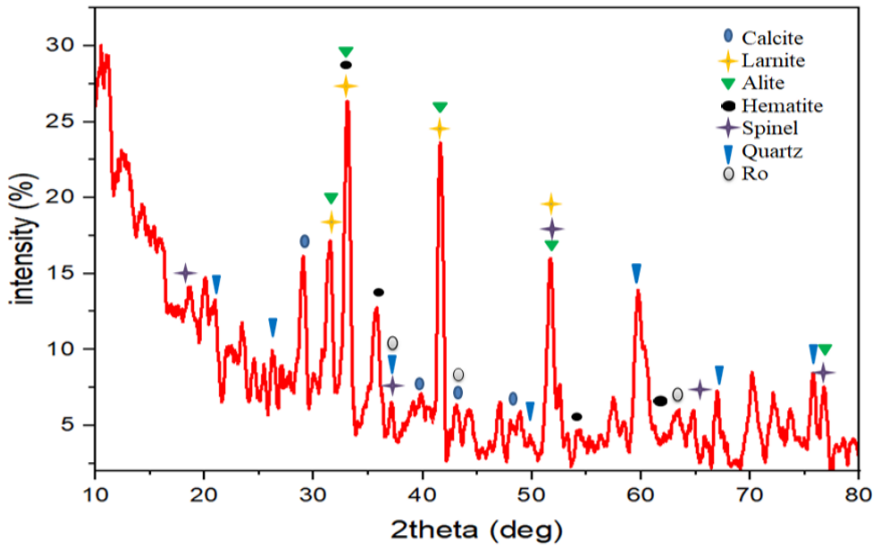

Figure 5: X-ray diffraction of steel slag aggregate

The dominant crystalline constituents of the steel slag sample include Calcite ($CaCO_3$, PDF# 01-072-1937), Larnite (β-Ca_2SiO_4, PDF# 00-033-0302), and Alite (C_3S, PDF# 00-049-0442). The presence of these calcium silicates aligns with the high concentrations of CaO and SiO_2 observed in the corresponding X-ray fluorescence (XRF) analysis. Calcite was identified by its main peak at 29.07°, with additional reflections at 39.43°, 43.17°, and 47.50°. Larnite exhibited a primary diffraction peak at

31.48°, along with overlaps with Alite at 32.5°, 41.16°, and 51.25°, while Alite was also identified by a characteristic peak at 33.63°. Furthermore, Hematite (Fe_2O_3, PDF# 00-033-0664) was identified as a major phase, consistent with the substantial iron content indicated by the XRF data. It exhibited diffraction peaks at 33.07°, 35.64°, 54.12°, and 62.47°. Additional phases include Magnesium Aluminate Spinel ($MgAl_2O_4$, PDF# 00-021-1152), which was confirmed by peaks at 51.78°, 36.85°, 65.12°, 18.35°, and 77.5°, correlating with the presence of both MgO and Al_2O_3 in the slag. Several minor peaks observed at 20.85°, 26.66°, 36.54°, 50.12°, 60.50°, 68.0°, and 75.6° were assigned to Quartz (SiO_2, PDF# 00-005-0490), further supporting the significant silicon content detected through XRF. A distinct feature attributed to the RO phase (PDF# 01-071-1179), a solid solution typically composed of divalent oxides such as CaO, MgO, FeO, and MnO, was observed with peaks at 42.9°, 62.3°, 36.0°, and 73.4°. The identification of this phase is characteristic of steel slags, particularly those produced in electric arc furnace (EAF) operations, and corroborates the dominant CaO and FeO presence in the chemical composition. These findings are in strong agreement with previous studies on EAF steel slags [34, 53-55]. The crystalline structure suggests limited reactivity of steel slag as a binder in geopolymers; thus, it is employed in this study as a substitute for aggregates, owing to its elevated iron oxide and reduced amorphous silica content.

The XRD diffractogram of the GPC, as shown in Figure 6, reveals a broad amorphous hump centered between 23–33°, which is characteristic of the formation of the geopolymeric gel Sodium Aluminosilicate Hydrate (NASH). This broad peak signifies the predominantly amorphous nature of the geopolymer matrix, a typical feature of geopolymer materials due to their disordered aluminosilicate network. The absence of sharp crystalline peaks in this region further confirms that the geopolymerization reaction has successfully transformed the MK-800 into an amorphous binding phase [56, 57].

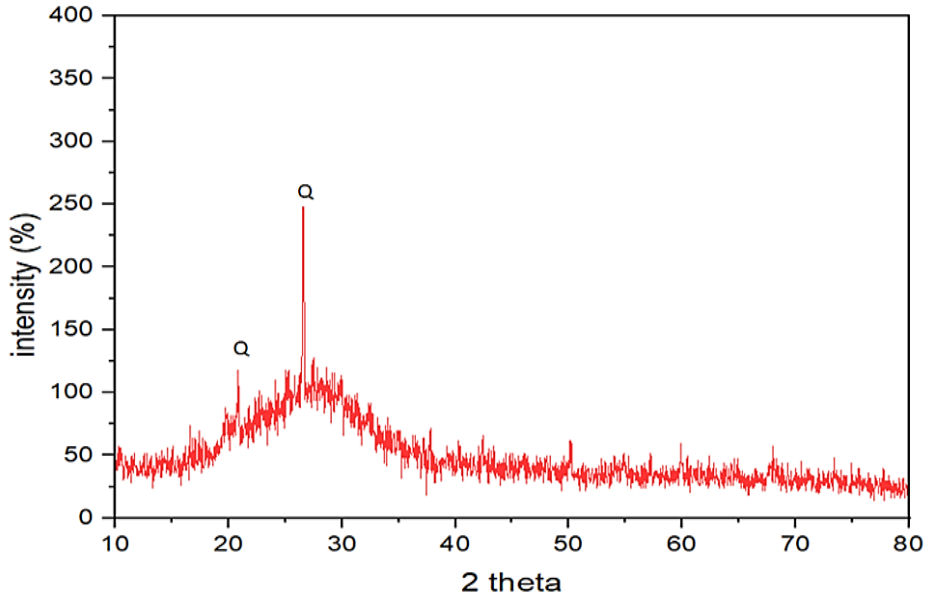

Figure 6: X-ray diffraction of GPC

3.2 FTIR Patterns

Figure 7 presents the FTIR spectra of raw kaolin and MK-800 after calcination. In the kaolin spectrum, the characteristic absorption bands at 3692, 3650, and 3620 cm^{-1} are attributed to the O–H stretching vibrations of the inner-surface hydroxyl groups. The band observed at 910 cm^{-1} corresponds to the Al–OH bending vibration. Additionally, the bands at 1004, 1026, and 1114 cm^{-1} are associated with Si–O stretching vibrations [58]. Peaks at 792 and 679 cm^{-1} are indicative of quartz vibrational modes [59], aligning with the crystalline phases identified in the XRD analysis. After calcination at 800 °C, the disappearance of the O–H stretching bands confirms the dehydroxylation of kaolinite and its transformation into amorphous metakaolin. These findings, in conjunction with the XRD results, demonstrate that thermal treatment at 800 °C is sufficient to achieve the complete conversion of kaolin into metakaolin.

The FTIR spectrum in Figure 8 reveals absorption bands at 704 cm^{-1} and 668 cm^{-1}, which are attributed to Si–O–Si bending vibrations, indicating the presence of silicate phases such as Larnite (β-Ca_2SiO_4, C_2S), and Alite (Tricalcium silicate, C_3S) [60]. These bands confirm the coexistence of calcium silicate and silicate minerals, which is consistent with the elevated SiO_2 and CaO concentrations identified through XRF analysis. The absorption band at 823 cm^{-1} corresponds to the Si–O stretching vibrations specifically associated with β-C_2S (Larnite) and Quartz, further substantiating the presence of this cementitious phase [61]. A prominent band at 668 cm^{-1} is also indicative of Fe–O stretching vibrations, suggesting the presence of iron-rich crystalline phases, such as Magnesioferrite ($MgFe_2O_4$) and Hematite (Fe_2O_3) [62]. This observation is in agreement with the significant Fe_2O_3 content revealed by the chemical analysis. The absorption band at 879 cm^{-1} is characteristic of C–O asymmetric bending vibrations (CO_3^{2-}), indicating the presence of Calcite ($CaCO_3$) [53, 63]. Additionally, the doublet observed at 2341 cm^{-1} and 2358 cm^{-1} corresponds to the asymmetric stretching vibrations of CO_2 molecules, which may be attributed to mechanical decomposition of calcite during sample preparation or atmospheric carbonation [64].

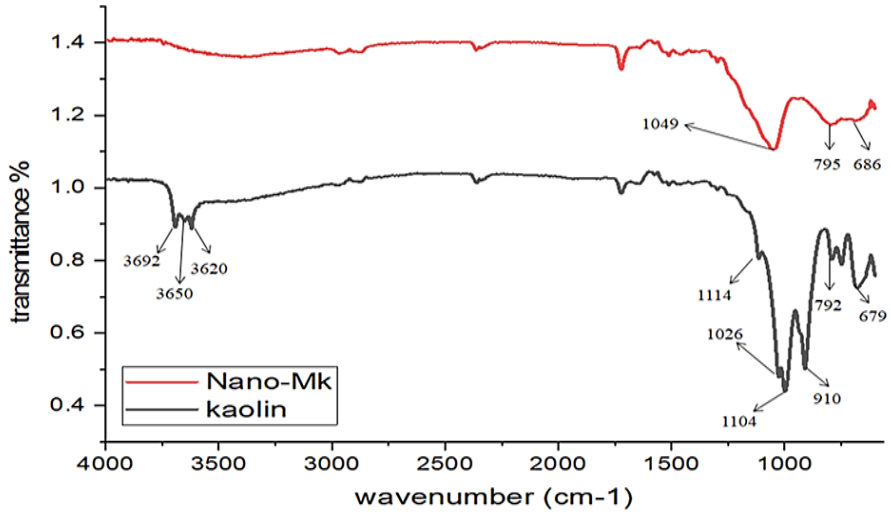

Figure 7: FT-IR spectrum of kaolin and MK-800

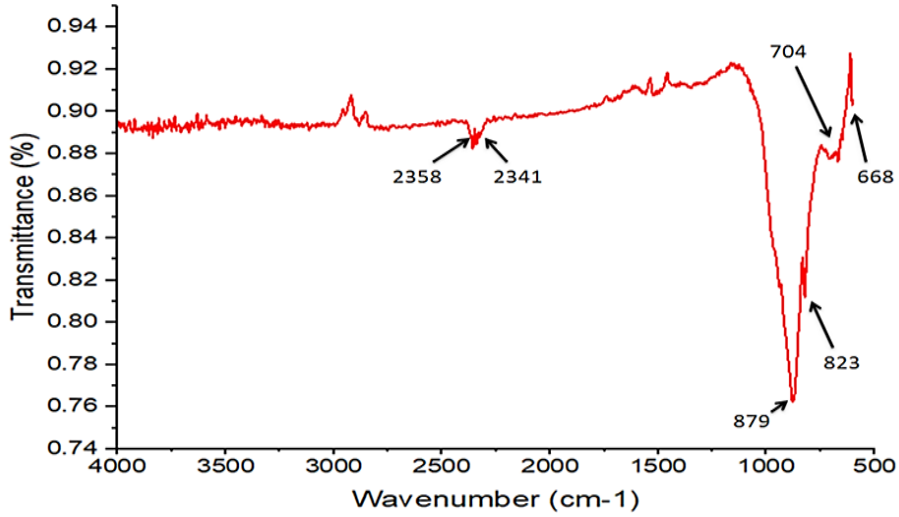

Figure 8: FT-IR spectrum of steel slag aggregate

3.3 Compressive strength

The mechanical strength of GPC is critically influenced by aggregates, which constitute 70–75% of the mixture mass. The compressive strength test results for the GP-0RCSA and GP-RCSA mixtures, which include RCSA, were assessed at both 7 and 28 days, as illustrated in Figure 9.

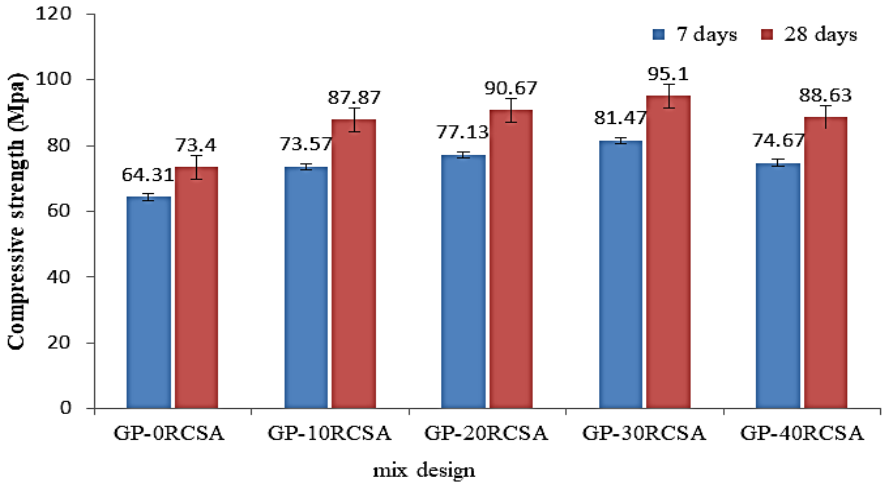

Figure 9: Compressive strength of GP-RCSA mixes at 7 and 28 days

For the mixes GP-10RCSA, GP-20RCSA, GP-30RCSA, and GP-40RCSA, the results showed compressive strength values of 73.57 MPa, 77.13 MPa, 81.47 MPa, and 74.67 MPa at 7 days, respectively. This corresponds to strength increases of 14.4%, 19.93%, 26.68%, and 16.11%, respectively. In comparison, the GP-0RCSA mix recorded a compressive strength of 64.31 MPa at the same age. At 28 days, the GPC incorporating varying proportions of RCSA (10%, 20%, 30%, and 40%) achieved compressive strengths of 87.87 MPa, 90.67 MPa, 95.1 MPa, and 88.63 MPa, respectively, reflecting increases of 19.71%, 23.53%, 29.56%, and 20.75%**.** The data imply that a replacement rate of approximately 30% is most suitable for producing GP-RCSA.

The enhancement in mechanical strength is mainly due to a strengthened interfacial transition zone, where the high lime content in RCSA facilitates the hydration of soluble Ca^{2+} ions adhered to the surface of RCSA. These ions subsequently form chemisorptive bonds with Si and Al in the GPC [38], resulting in the formation of C-A-S-H gel. This gel contributes to strength enhancement in two ways: firstly, by serving as nucleation sites that accelerate geopolymerization [65-67]. Secondly, the coexistence of C-A-S-H gel with N-A-S-H gel enables their interconnection, which in turn enhances the structure of the pore. These interconnected gels on the surface of RCSA substantially strengthen the interfacial adhesion between the RCSA and the paste [68, 69]. In addition, the higher water absorption capacity of RCSA contributes to its ability to hold moisture, which facilitates continued hydration and strengthens the bond between the aggregates and the geopolymer paste [70]. Additionally, the superior mechanical strength of RCSA compared to NCA, with a Mohs hardness rating between 6 and 7 [71,72] It also plays a crucial role in this enhancement [18].

3.4 Splitting tensile strength

As illustrated in Figure 10, the partial substitution of NCA with RCSA led to an improvement in splitting tensile strength for both 7-day and 28-day, reflecting a similar trend observed in the compressive strength results.

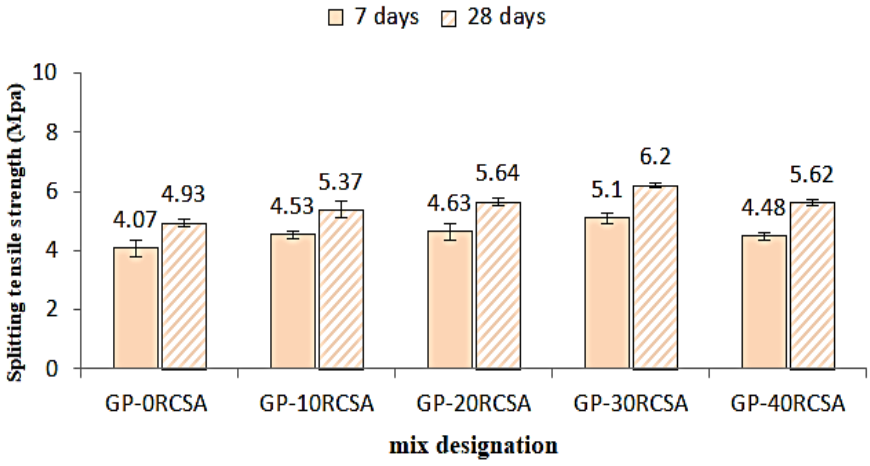

Figure 10: Splitting tensile strength of GP-RCSA mixes at 7 and 28 days

According to the results, the tensile Strength at 7 days of curing for GP-10RCSA, GP-20RCSA, GP-30RCSA, and GP-40RCSA was 4.53 MPa, 4.63 MPa, 5.1 MPa, and 4.48 MPa, respectively, which is about 11.3 %, 13.76 %, 25.31% and 10.07 % higher than 4.07 MPa recorded for GP-0RCSA at the same age. In comparison to the tensile Strength at 7 days, a notable improvement in the tensile Strength value at 28 days, with (5.37, 5.64, 6.2, 5.62) MPa, for 10%,20%,30%,40% RCSA replacement, is recorded. Concerning the results recorded, the highest recorded value is for GP-30RCSA, followed by a small reduction in value for GP-40RCSA. This enhancement may result from the increased adhesion between the geopolymer paste and the RCSA aggregate, which is likely due to the uneven form and rough surface texture of the RCSA [73, 74], with Surface pores measuring between 0.01 and 10 micrometers in diameter [75]. Since the GPC splitting tensile strength is significantly influenced by the surface roughness and angularity of the aggregates, as these factors enhance mechanical interlocking and frictional resistance at the aggregate-binder interface, thereby improving the overall bond strength within the composite matrix [76]. The other reason for the enhancement is the diffusion of free lime from the RCSA to the GP paste, forming a denser interfacial zone.

3.5 Flexural strength

The flexural strength at two curing ages (7 and 28 days) was evaluated on prism specimens using a three-point bending test. The flexural strength of the GP-RCSA mixes exhibited a similar trend to their compressive and tensile strengths.

It can be deduced from Figure 11 that the GP-10RCSA, GP-20RCSA, GP-30RCSA, and GP-40RCSA mixtures measured flexural strength of 8.43 MPa, 8.99 MPa, 9.53 MPa, and 8.73 MPa at 7 days, respectively, while the GP-0RCSA recorded a value of 6.57 MPa at the same age. By 28 days, the flexural strength of the RA-RCWGP concrete showed a significant increase with values of approximately 9.77 MPa, 10.1 MPa, 11.3 MPa, and 9.64 MPa, indicating that RCSA significantly affected the flexural strength. With 30% RCSA substitution, the GP-30RCSA mixture exhibited the maximum flexural strength of more than 11.13 MPa, achieving an improvement of 41.4% compared to GP-0RCSA. Although GP-40RCSA exhibited a decline in flexural strength, it still surpassed that of the GP-0RCSA mixture. The increased flexural strength may be explained by the enhanced ductility of the RCSA coarse aggregates, which is largely a result of their elevated iron content. Furthermore, the superior bonding

between the RCSA aggregates and the geopolymer paste plays a crucial role, owing to the aggregates' porous texture and pronounced angularity [77].

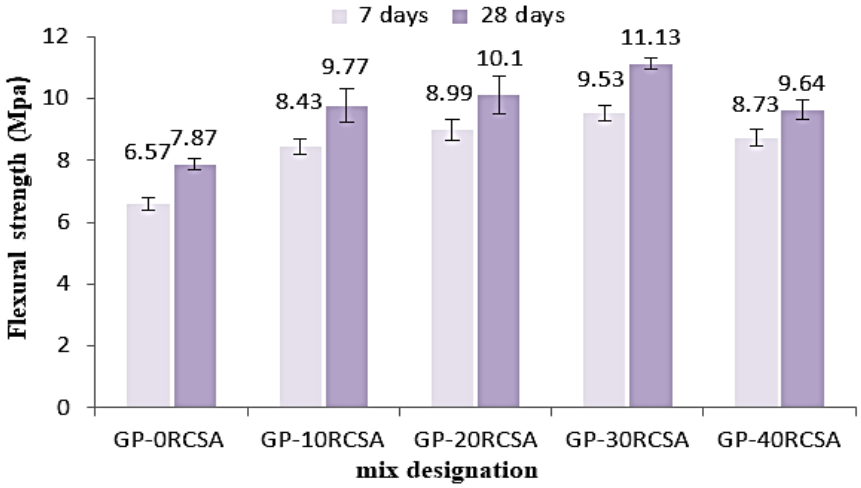

Figure 11: Flexural strength of GP-RCSA mixes at 7 and 28 days

3.6 Bulk density

The density of the aggregates largely influences Bulk Density, as they constitute more than 70% of the total GPC mass. It can be deduced from Figure 12 that a notable increase in bulk density is observed for mixtures containing RCSA. At 7 days, the bulk densities of the GP-10RCSA, GP-20RCSA, GP-30RCSA, and GP-40RCSA mixes were recorded as 1980.93 kg/m³, 2034.48 kg/m³, 2088.68 kg/m³, 2156.7 kg/m³, which further increased to 2204.37 kg/m³, 2260.23 kg/m³, 2316.09 kg/m³, and 2371.96 kg/m³ by 28 days. The bulk density consistently rose with increasing percentages of RCSA replacement, attributed to the greater specific gravity of RCSA compared to NCA, with RCSA having a specific gravity of 3.31. In contrast, NCA has a specific gravity of 2.56.

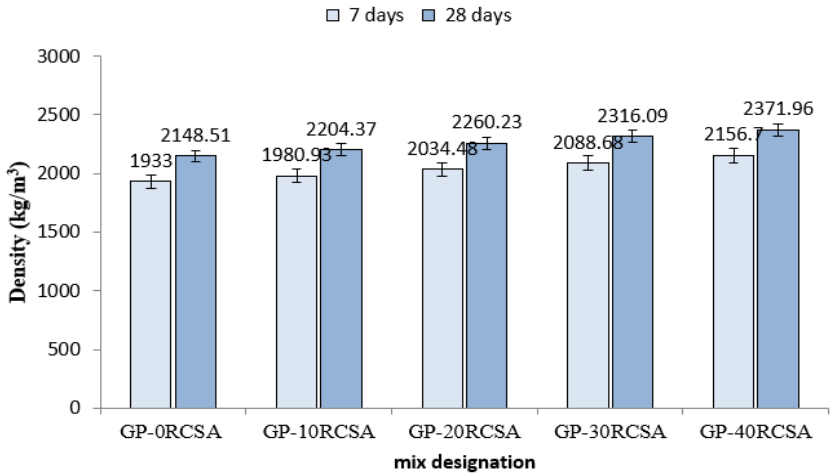

Figure 12: Bulk density of GP-RCSA mixes at 7 and 28 days

3.7 Percentage of permeable voids

The porosity of GPC directly influences both its strength and permeability, making it a critical factor in determining the material's overall properties. In this study, the incorporation of different proportions of RCSA (10, 20, 30, and 40%) resulted in a decline in the porosity of GP-RCSA to 11.95, 11.2, 10.77, and 10.95%, respectively, compared to the GP-0RCSA mix (13.4%) at 7 days. A continuous decline is noted with the curing time at 28 days with a porosity of 10.37, 10.1, 9.3, and 9.5% for GP-10RCSA, GP-20RCSA, GP-30RCSA, and GP-40RCSA, respectively, as can be seen in Figure 13.

The observed decrease in porosity can be attributed to several mechanisms. Primarily, the absorption of free lime by the low-calcium geopolymer paste plays a key role. As the free lime is absorbed, it diffuses away from the interfacial transition zone, promoting the formation of C-S-H gels. These gels effectively fill the voids, bonding the adjacent solid phases together and resulting in the formation of a more continuous and dense interfacial transition zone [38]. Additionally, the calcium ions present in the RCSA may interact with the geopolymer matrix, entering the N-A-S-H gel structure and partially replacing sodium ions without disrupting the gel's chain structure. This replacement further enhances the formation of a robust and dense structure, which is likely to contribute to the improved porosity characteristics of the GPC.

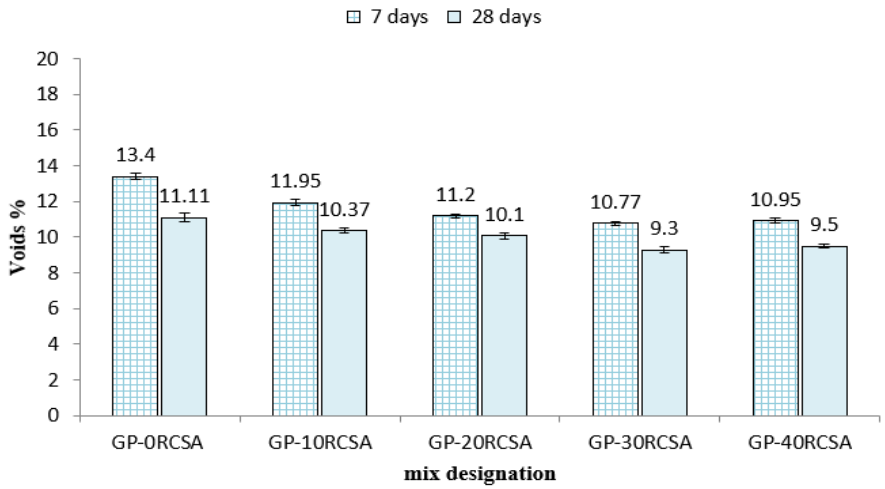

Figure 13: Porosity % of GP-RCSA mixes at 7 and 28 days

Supporting this, a study conducted by Sun et al. [78] demonstrated that an increased Ca/Si ratio, particularly in the interfacial transition zone, suggests the diffusion of calcium ions toward the geopolymer paste. The presence of these calcium ions within the ITZ may help to accumulate around the interface, improving the overall density and integrity of the matrix, and contributing to the reduction in porosity.

3.8 Water absorption

To evaluate the durability and performance of GPC under harsh conditions, water absorption testing was employed as a reliable and effective evaluation method [79]. Water absorption is defined by several factors, such as the interfacial transition zone, pore structure, and paste pores [80].

The results, as shown in Figure 14, suggest a slight decrease in the water absorption of the GP-RCSA mixes, even though RCSA exhibits significantly higher water absorption compared to NCA due to its highly porous surface structure. This phenomenon can be attributed to the geopolymer paste effectively encapsulating the pores within the RCSA, thereby forming a denser interfacial transition zone that substantially improves the resistance of GPC to water ingress, thus improving the ability of the geopolymer paste to encapsulate the pores in RCSA, thus enhancing the interfacial transition zone and improving its resistance to water ingress [81]. Quantitatively, the GP-10RCSA, GP-20RCSA, GP-30RCSA, and GP-40RCSA mixes demonstrate reductions in water absorption of 5.52, 5.22, 5.10, and 5.28%, respectively, compared to the GP-0RCSA mix at 7 days. These reductions become even more pronounced at 28 days, with corresponding decreases of 4.57, 4.48, 4.3 and 4.50%, compared to the GP-0RCSA mix (4.74%). These findings underscore the enhanced impermeability of GPC incorporating recycled steel slag coarse aggregates, highlighting its potential for improved durability in demanding service conditions.

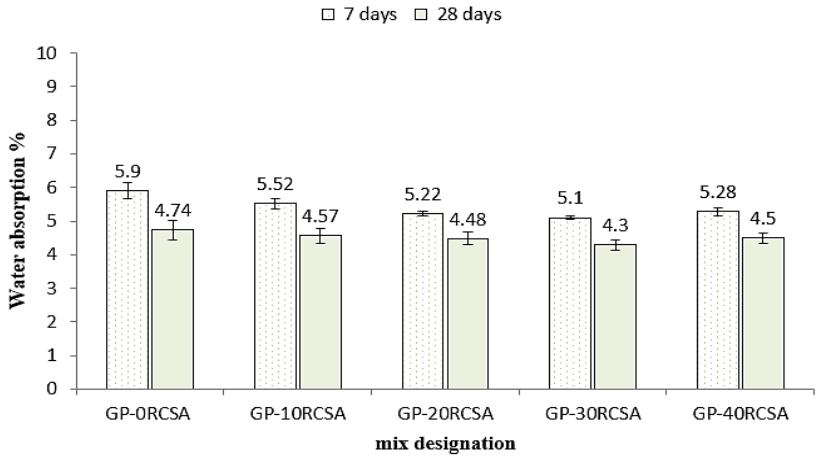

Figure 14: Water absorption of GP-RCSA mixes at 7 and 28 days

4. Conclusion

This study successfully demonstrates that RCSA can be effectively utilized as a sustainable alternative to NCA in metakaolin-based GPC and significantly improves the mechanical and physical properties of the GPC. The findings highlight that all GP-RCSA, which contain different percentages of RCSA, have significant mechanical properties as compared with the control sample (without RCSA addition), with an optimal RCSA incorporation (30% replacement), achieving 29.56% higher compressive strength (95.1 MPa), 25.31% (6.2 MPa) greater tensile strength, and 41.4% (11.13 MPa) enhanced flexural strength

compared to the reference material. These gains are attributed to RCSA's high calcium content, which promotes the formation of a denser interfacial transition zone (ITZ) through C-A-S-H/N-A-S-H gel coexistence. Additionally, RCSA incorporation reduced the Volume of Permeable Voids by 26.32% and water absorption by 9.18%, enhancing durability. The higher bulk density (2371.96 kg/m³) further underscores RCSA's role in improving concrete performance. Microstructural analyses confirmed the formation of a robust amorphous geopolymer network. Environmentally, this approach mitigates steel slag waste, reduces reliance on natural aggregates, and lowers CO_2 emissions, aligning with sustainable construction goals. Future research should explore long-term durability under real-world conditions to facilitate broader industrial adoption of RCSA-based GPC.

Author contributions

Conceptualization, **R. Jaddan** and **H. Jaber**; data curation, **R. Jaddan** and **H. Jaber**.; formal analysis **R. Jaddan** and **H. Jaber**.; investigation, **R. Jaddan** and **H. Jaber**.; methodology, **R. Jaddan** and **H. Jaber**.; writing—original draft preparation, **R. Jaddan** and **H. Jaber**.; writing—review and editing, **R. Jaddan** and **H. Jaber**. All authors have read and agreed to the published version of the manuscript.

Funding

This research received no specific grant from any funding agency in the public, commercial, or not-for-profit sectors.

Data availability statement

The data that support the findings of this study are available on request from the corresponding author.

Conflicts of interest

The authors declare that there is no conflict of interest.

References

[1] P. J. M. Monteiro, S.A. Miller, A. Horvath, Towards sustainable concrete, Nat. Mater., 16 (2017) 698-699. https://doi.org/10.1038/nmat4930

[2] M. Soomro, V. W. Y. Tam, A. C. J. Evangelista, 2023. 2 - Production of cement and its environmental impact, Recycled Concrete Technologies and Performance Woodhead Publishing Series in Civil and Structural Engineering, pp. 11–46. https://doi.org/10.1016/B978-0-323-85210-4.00010-2

[3] A. T. Azeez, M. S. Hassan, A. A. H. Attiyah, Modelling the complementary role of inert slag aggregate and waste glass on concrete mechanical strengths using the response surface and design-of-experiment approach, Constr. Build. Mater., 409 (2023) 134199. https://doi.org/10.1016/j.conbuildmat.2023.134199

[4] N. A. Madlool, R. Saidur, M.S. Hossain, N.A. Rahim, A critical review of energy use and savings in the cement industries, Renewable Sustainable Energy Rev., 15 (2011) 2042-2060. https://doi.org/10.1016/j.rser.2011.01.005

[5] J.-F. Xie, Y.-X. Huang, W.-W. Li, X.-N. Song, L. Xiong, H.-Q. Yu, Efficient electrochemical CO_2 reduction on a unique chrysanthemum-like Cu nanoflower electrode and direct observation of carbon deposite, Electrochim. Acta, 139 (2014) 137-144. https://doi.org/10.1016/j.electacta.2014.06.034

[6] J. Wei, K. Cen, Empirical assessing cement CO_2 emissions based on China's economic and social development during 2001–2030, Sci. Total Environ., 653 (2019) 200-211. https://doi.org/10.1016/j.scitotenv.2018.10.371

[7] S. Nie, Q. Zhang, M. Lan, J. Zhou, M. Xu, H. Li, J. Wang, Fundamental design of low-carbon ordinary Portland cement-calcium sulfoaluminate clinker-anhydrite blended system, Cem. Concr. Compos., 139 (2023) 105053. https://doi.org/10.1016/j.cemconcomp.2023.105053

[8] A. Sharma, N.Basumatary, P.Singh, K.Kapoor, S.P. Singh, Potential of geopolymer concrete as substitution for conventional concrete: A review, Mater. Today Proc., 57 (2022) 1539-1545. https://doi.org/10.1016/j.matpr.2021.12.159

[9] M. Amran, A. Al-Fakih, S. H. Chu, R. Fediuk, S. Haruna, A. Azevedo, N. Vatin, Long-term durability properties of geopolymer concrete: An in-depth review, Case Stud. Constr. Mater., 15 (2021) e00661. https://doi.org/10.1016/j.cscm.2021.e00661

[10] W. Li, E.D. Shumuye, T. Shiying, Z. Wang, K. Zerfu, Eco-friendly fibre reinforced geopolymer concrete: A critical review on the microstructure and long-term durability properties, Case Stud. Constr. Mater., 16 (2022) e00894. https://doi.org/10.1016/j.cscm.2022.e00894

[11] Q. J. Frayyeh, W. I. Khalil, H. T. Abed, Sustainable metakaolin based pervious geopolymer concrete with recycled concrete aggregate, 4th International Conference on Buildings, Construction and Environmental Engineering, 737, 2020, 012049. https://dx.doi.org/10.1088/1757-899X/737/1/012049.

[12] B. Al-Shathr, M. Shamsa, T. Al-Attar, Relationship between amorphous silica in source materials and compressive strength of geopolymer concrete, The 3rd International Conference on Buildings, Construction and Environmental Engineering, 162, 2018, 02019. https://doi.org/10.1051/matecconf/201816202019.

[13] A. J. Abed Al-Jabar, S.I.Ibrahim, H.A. Al-Kaisy, Factors affect the bond strength of Geopolymer repair material: Review, 3rd International Scientific Conference of Engineering Sciences and Advances Technologies, 1973, 2021, 012134. https://dx.doi.org/10.1088/1742-6596/1973/1/012134.

[14] S. A. Abukersh, C.A.Fairfield, Recycled aggregate concrete produced with red granite dust as a partial cement replacement, Constr. Build. Mater., 25 (2011) 4088-4094. https://doi.org/10.1016/j.conbuildmat.2011.04.047

[15] T. Huang, D. Song, L. Zhou, L. Pan, S.-w. Zhang, Self-alkali-activated self-cementation achievement and mechanism exploration for the synergistic treatment of the municipal solid waste incineration fly ashes and the arsenic-contaminated soils, Chemosphere, 325 (2023) 138397. https://doi.org/10.1016/j.chemosphere.2023.138397

[16] Wang, G. C., The utilization of slag in civil infrastructure construction, Woodhead Publishing, 2016.

[17] F. K. Abd, W. I. Khalil, A. A. Jaber, Production of sustainable concrete with treated cement kiln dust and iron slag waste aggregate, Open Eng., 14 (2024)1-11. https://doi.org/10.1515/eng-2024-0014.

[18] Z. Ren, D. Li, Application of Steel Slag as an Aggregate in Concrete Production: A Review, Materials, 16 (2023) 5841. https://www.mdpi.com/1996-1944/16/17/5841.

[19] W. Guo, B. Xi, C. Huang, J. Li, Z. Tang, W. Li, C. Ma, W. Wu, Solid waste management in China: Policy and driving factors in 2004–2019, Resour. Conserv. Recycl., 173 (2021) 105727. https://doi.org/10.1016/j.resconrec.2021.105727

[20] X. Zhang, H. Li, S. Li, Y. Ding, H. Zhang, Y. Tong, S. Hua, Test and Microstructural Analysis of a Steel Slag Cement-Based Material Using the Response Surface Method, Materials, 15 (2022) 3114. https://doi.org/10.3390/ma15093114

[21] X. Zhang, C. Qian, Z. Ma, F. Li, Study on preparation of supplementary cementitious material using microbial CO2 fixation of steel slag powder, Constr. Build. Mater., 326 (2022) 126864. https://doi.org/10.1016/j.conbuildmat.2022.126864

[22] M. Salman, Ö. Cizer, Y. Pontikes, L. Vandewalle, B. Blanpain, K. Van Balen, Effect of curing temperatures on the alkali activation of crystalline continuous casting stainless steel slag, Constr. Build. Mater., 71 (2014) 308-316. https://doi.org/10.1016/j.conbuildmat.2014.08.067

[23] X.-d. Xiang, J.-c. Xi, C.-h. Li, X.-w. Jiang, Preparation and application of the cement-free steel slag cementitious material, Constr. Build. Mater., 114 (2016) 874-879. https://doi.org/10.1016/j.conbuildmat.2016.03.186

[24] O. Najm, H. El-Hassan, A. El-Dieb, Ladle slag characteristics and use in mortar and concrete: A comprehensive review, J. Cleaner Prod., 288 (2021) 125584. https://doi.org/10.1016/j.jclepro.2020.125584

[25] W. Gao, W. Zhou, X. Lyu, X. Liu, H. Su, C. Li, H.Wang, Comprehensive utilization of steel slag: A review, Powder Technol., 422 (2023) 118449. https://doi.org/10.1016/j.powtec.2023.118449

[26] A. A. Nugraha, M. Fauziah, Subarkah, The Use of Steel Slag as Substitution of Coarse Aggregate on Indirect Tensile Strength and Marshall Properties of AC-WC, 6th International Conference on Sustainable Built Environment, 933, 2021,012004. https://dx.doi.org/10.1088/1755-1315/933/1/012004

[27] Z. M. Abed, H. K. Ahmed, W. I. Khalil, Optimization of Silica Fume and Slag in Roller Compacted Concrete by Taguchi Method, Eng. Technol. J., 41 (2023) 724-733. http://doi.org/10.30684/etj.2023.138600.1411

[28] A. J. Mohammed, M. S. Hassan, H. Al-Quraishi, Synergistic effect of nano-silica, steel slag, and waste glass on the microstructure, electrical resistivity, and strength of ultra-high-performance concrete, Open Eng., 15 (2025). https://doi.org/10.1515/eng-2024-0105.

[29] M. H. Lai, J. Zou, B. Yao, J. C. M. Ho, X. Zhuang, Q. Wang, Improving mechanical behavior and microstructure of concrete by using BOF steel slag aggregate, Constr. Build. Mater., 277 (2021) 122269. https://doi.org/10.1016/j.conbuildmat.2021.122269

[30] Q. Wang, D. Wang, S. Zhuang, The soundness of steel slag with different free CaO and MgO contents, Constr. Build. Mater., 151 (2017) 138-146. https://doi.org/10.1016/j.conbuildmat.2017.06.077

[31] I. A. Altun, İ. Yılmaz, Study on steel furnace slags with high MgO as additive in Portland cement, Cem. Concr. Res., 32 (2002) 1247-1249. https://doi.org/10.1016/S0008-8846(02)00763-9

[32] A. S. Brand, and J. R. Roesler, Steel furnace slag aggregate expansion and hardened concrete properties, Cem. Concr. Compos., 60 (2015) 1-9. https://doi.org/10.1016/j.cemconcomp.2015.04.006

[33] G. Wang, Determination of the expansion force of coarse steel slag aggregate, Constr. Build. Mater., 24 (2010) 1961-1966. https://doi.org/10.1016/j.conbuildmat.2010.04.004

[34] P. E. Tsakiridis, G. D. Papadimitriou, S. Tsivilis, C. Koroneos, Utilization of steel slag for Portland cement clinker production, J. Hazard. Mater., 152 (2008) 805-811. https://doi.org/10.1016/j.jhazmat.2007.07.093

[35] T. Bai, Z.-G. Song, Y.-G. Wu, X.-D. Hu, H. Bai, Influence of steel slag on the mechanical properties and curing time of metakaolin geopolymer, Ceram. Int., 44 (2018) 15706-15713. https://doi.org/10.1016/j.ceramint.2018.05.243

[36] R. I. Iacobescu, D. Koumpouri, Y. Pontikes, R. Saban, G. N. Angelopoulos, Valorisation of electric arc furnace steel slag as raw material for low energy belite cements, J. Hazard. Mater., 196 (2011) 287-294. https://doi.org/10.1016/j.jhazmat.2011.09.024

[37] O. Ibrahim, A. Heniegal, G. Elhameed, H. Mohamadien, Effect of Local Steel Slag as a Coarse Aggregate on Properties of Fly Ash Based-Geopolymer Concrete, Int. J. Civ. Environ. Struct. Constr. Archit. Eng., 9 (2015) 1452- 1460 .

[38] M. S. H. Khan, A. Castel, A. Akbarnezhad, S. J. Foster, M. Smith, Utilisation of steel furnace slag coarse aggregate in a low calcium fly ash geopolymer concrete, Cem. Concr. Res., 89 (2016) 220-229. https://doi.org/10.1016/j.cemconres.2016.09.001

[39] A. H. Mahmood, S. J. Foster, A. Castel, High-density geopolymer concrete for Port Kembla breakwater upgrade, Constr. Build. Mater., 262 (2020) 120920. https://doi.org/10.1016/j.conbuildmat.2020.120920

[40] A. H. Mahmood, S. J. Foster, A. Castel, Development of high-density geopolymer concrete with steel furnace slag aggregate for coastal protection structures, Constr. Build. Mater., 248 (2020) 118681. https://doi.org/10.1016/j.conbuildmat.2020.118681

[41] N. Suganya, S. T. T., Durability of Geopolymer Concrete with Scrap Steel Slag Coarse Aggregate, Int. J. Eng. Adv. Technol., 9 (2020) 2415- 2417. https://doi.org/10.35940/ijeat.C4673.029320

[42] A. Amani, A. M. Ramezanianpour, M. Palassi, Investigation on the sustainable use of electric arc furnace slag aggregates in eco-friendly alkali-activated low fineness slag concrete as a green construction composite, J. Cleaner Prod., 307 (2021) 127257. https://doi.org/10.1016/j.jclepro.2021.127257

[43] Q. Wan, F. Rao, S. Song, Reexamining calcination of kaolinite for the synthesis of metakaolin geopolymers - roles of dehydroxylation and recrystallization, J. Non-Cryst. Solids, 460 (2017) 74-80. https://doi.org/10.1016/j.jnoncrysol.2017.01.024

[44] H. Owaid, Z. A. S. Ghali, S.A. Ali, Compressive strength, ultrasonic pulse velocity and transport properties of self-compacting high performance concrete made with iraqi metakaolin, Int. J. Civ. Eng.Technol., 9 (2018) 31-44.

[45] F. A. Shilar, S. V. Ganachari, V. B. Patil, T. Y. Khan, S. D. A. Khadar, Molarity activity effect on mechanical and microstructure properties of geopolymer concrete: A review, Case Stud. Constr. Mater., 16 (2022) e01014. http://dx.doi.org/10.1016/j.cscm.2022.e01014

[46] Iraqi-Specification-No. 45, Aggregate from natural sources for concrete and construction, in Aggregate from natural sources for concrete and construction, Central Organization for Standardization and Quality Control Iraq, 2016.

[47] J. Xie, O. Kayali, Effect of initial water content and curing moisture conditions on the development of fly ash-based geopolymers in heat and ambient temperature, Constr. Build. Mater., 67 (2014) 20-28. https://doi.org/10.1016/j.conbuildmat.2013.10.047

[48] BS 1881-116; Testing concrete - Method for determination of compressive strength of concrete cubes, BSI: London, UK, 2004.

[49] ASTM C293/C293M; Standard Test Method for Flexual Strength of Concrete (Using Simple Beam with Center-Point Loading) ASTM International: West Conshohocken: USA, 2016.

[50] ASTM C496; Standard Test Method for Splitting Tensile Strength of Cylindrical Concrete Specimens, ASTM International: West Conshohocken: USA, 2011.

[51] BS EN 12390-7; Testing hardened concrete - Density of hardened concrete, 2019.

[52] ASTM C642; Standard Test Method for Density, Absorption, and Voids in Hardened Concrete, ASTM International: West Conshohocken: PA, USA, 2013.

[53] X. Wang, W. Ni, J. Li, S. Zhang, K. Li, Study on Mineral Compositions of Direct Carbonated Steel Slag by QXRD, TG, FTIR, and XPS, Energies, 14 (2021) 4489. https://doi.org/10.3390/en14154489

[54] M. Herbelin, J. Bascou, V. Lavastre, D. Guillaume, M. Benbakkar, S. Peuble, J.-P. Baron, Steel Slag Characterisation—Benefit of Coupling Chemical, Mineralogical and Magnetic Techniques, Minerals, 10 (2020) 705. https://doi.org/10.3390/min10080705

[55] Y. Li, K. Guo, J. Xiang, G. Pei, X. Lv, Effect of Cooling Method on the Mineralogy and Stability of Steel Slag, ISIJ International, 62 (2022) 2197-2206. https://doi.org/10.2355/isijinternational.ISIJINT-2022-101

[56] M. Kaya, The effect of micro-SiO_2 and micro-Al_2O_3 additive on the strength properties of ceramic powder-based geopolymer pastes, J. Mater. Cycles Waste Manage., 24 (2022) 333-350. https://doi.org/10.1007/s10163-021-01323-3.

[57] B. Kim and S. Lee, Review on characteristics of metakaolin-based geopolymer and fast setting, J. Korean Ceram. Soc., 24 (2020) 368-377. https://doi.org/10.1007/s43207-020-00043-y.

[58] Farmer, V. C., The Infrared Spectra of Minerals, V. 4, Mineralogical Society of Great Britain and Ireland, 1974. http://dx.doi.org/10.1180/mono-4

[59] M. Criado, A. Fernández-Jiménez, A. Palomo, Alkali activation of fly ash: Effect of the SiO_2/Na_2O ratio: Part I: FTIR study, Microporous Mesoporous Mater., 106 (2007) 180-191. https://doi.org/10.1016/j.micromeso.2007.02.055

[60] I. A. Funmilayo, B. O. Mary, Synthesis of geopolymer binders and mortars from Ijero-Ekiti calcined clay, blast furnace slag and river sand, Earthline J. Chem. Sc., 4 (2020) 15-34 . https://doi.org/10.34198/ejcs.4120.1534

[61] L. Stefanini, S. Ghorbani, G. De Schutter, S. Matthys, B. Walkley, J. L. Provis, Evaluation of copper slag and stainless steel slag as replacements for blast furnace slag in binary and ternary alkali-activated cements, J. Mater. Sci., 58 (2023) 12537-12558. https://doi.org/10.1007/s10853-023-08815-7.

[62] D. A. Long, Infrared and Raman characteristic group frequencies. Tables and charts George Socrates John Wiley and Sons, Ltd, Chichester, Third Edition, 2001., J. Raman Spectrosc., 35 (2004) 905-905. https://doi.org/10.1002/jrs.1238

[63] F. Zhu, L. Cui, Y. Liu, L. Zou, J. Hou, C. Li, G. Wu, R. Xu, B. Jiang, Z. Wang, Experimental Investigation and Mechanism Analysis of Direct Aqueous Mineral Carbonation Using Steel Slag, Sustainability, 16 (2024) 81. https://www.mdpi.com/2071-1050/16/1/81.

[64] S. P. Pinnelli, K. Prasad, N. Thakur, FTIR signatures of type-II clathrates of carbon dioxide in natural quartz veins, Curr. Sci., 90 (2006).

[65] C. K. Yip, G. C. Lukey, J. L. Provis, J. S. J. van Deventer, Effect of calcium silicate sources on geopolymerisation, Cem. Concr. Res., 38 (2008) 554-564. https://doi.org/10.1016/j.cemconres.2007.11.001

[66] S. Puligilla ,P. Mondal, Role of slag in microstructural development and hardening of fly ash-slag geopolymer, Cem. Concr. Res., 43 (2013) 70-80. https://doi.org/10.1016/j.cemconres.2012.10.004

[67] J. Temuujin, A. van Riessen, R. Williams, Influence of calcium compounds on the mechanical properties of fly ash geopolymer pastes, J. Hazard. Mater., 167 (2009) 82-88. https://doi.org/10.1016/j.jhazmat.2008.12.121

[68] S. A. Bernal, E. D. Rodríguez, R. Mejía de Gutiérrez, M. Gordillo, J.L. Provis, Mechanical and thermal characterisation of geopolymers based on silicate-activated metakaolin/slag blends, J. Mater. Sci., 46 (2011) 5477-5486. https://doi.org/10.1007/s10853-011-5490-z.

[69] X. Guo , X. Pan, Effects of Steel Slag on Mechanical Properties and Mechanism of Fly Ash–Based Geopolymer, J. Mater. Civ. Eng., 32 (2020) 04019348. https://doi.org/10.1061/(ASCE)MT.1943-5533.0003012

[70] M. H. Lai, Z. H. Chen, Y. H. Wang, J. C. M. Ho, Effect of fillers on the mechanical properties and durability of steel slag concrete, Constr. Build. Mater., 335 (2022) 127495. https://doi.org/10.1016/j.conbuildmat.2022.127495

[71] D. Mombelli, C. Mapelli, A. Gruttadauria, C. Baldizzone, F. Magni, P. L. Levrangi, and P. Simone, Analisys of Electric Arc Furnace Slag, Steel Res. Int., 83 (2012) 1012-1019. https://doi.org/10.1002/srin.201100259

[72] M. C. Arnold, A. S. de Vargas, L. Bianchini, Study of electric-arc furnace dust (EAFD) in fly ash and rice husk ash-based geopolymers, Adv. Powder Technol., 28 (2017) 2023-2034. https://doi.org/10.1016/j.apt.2017.05.007

[73] L. Rondi, G. Bregoli, S. Sorlini, L. Cominoli, C. Collivignarelli, G. Plizzari, Concrete with EAF steel slag as aggregate: A comprehensive technical and environmental characterization, Composites, Part B, 90 (2016) 195-202. https://doi.org/10.1016/j.compositesb.2015.12.022

[74] C. Pellegrino, V. Gaddo, Mechanical and durability characteristics of concrete containing EAF slag as aggregate, Cem. Concr. Compos., 31 (2009) 663-671. https://doi.org/10.1016/j.cemconcomp.2009.05.006

[75] S. Monosi, M. L. Ruello, D. Sani, Electric arc furnace slag as natural aggregate replacement in concrete production, Cem. Concr. Compos., 66 (2016) 66-72. https://doi.org/10.1016/j.cemconcomp.2015.10.004

[76] K.-R. Wu, B. Chen, W. Yao, D. Zhang, Effect of coarse aggregate type on mechanical properties of high-performance concrete, Cem. Concr. Res., 31 (2001) 1421-1425. https://doi.org/10.1016/S0008-8846(01)00588-9

[77] K. Kishore, M. N. Sheikh, M. N. S. Hadi, A critical analysis of electric arc furnace (EAF) slag for sustainable geopolymer concrete production, Mater. Today Sustainability, 29 (2025) 101064. https://doi.org/10.1016/j.mtsust.2024.101064

[78] K. Sun, X. Peng, S. H. Chu, S. Wang, L. Zeng, G. Ji, Utilization of BOF steel slag aggregate in metakaolin-based geopolymer, Constr. Build. Mater., 300 (2021) 124024. https://doi.org/10.1016/j.conbuildmat.2021.124024

[79] A. A. Hashim, R. Anaee, M.S. Nasr, Enhancing the sustainability, mechanical and durability properties of recycled aggregate concrete using calcium-rich waste glass powder as a supplementary cementitious material: An experimental study and environmental assessment, Sustainable Chem. Pharm., 44 (2025) 101985. https://doi.org/10.1016/j.scp.2025.101985

[80] A. A. Hashim, R. Anaee, M. S. Nasr, A. Shubbar, and T. S. Alahmari, Mechanical properties, corrosion resistance and microstructural analysis of recycled aggregate concrete made with ceramic wall waste and ultrafine ceria, J. Mater. Res. Technol., 36 (2025) 627-640. https://doi.org/10.1016/j.jmrt.2025.03.154

[81] E. Teymouri, K. S. Wong, Y. Y. Tan, N. N. M. Pauzi, Mechanical behaviour of adsorbent pervious concrete using iron slag and zeolite as coarse aggregates, Constr. Build. Mater., 388 (2023) 131720. https://doi.org/10.1016/j.conbuildmat.2023.131720